Title

Redshift weights for baryon acoustic oscillations: application to mock galaxy catalogues

Journal

Monthly Notices of the Royal Astronomical Society, 461(3)

ISSN

0035-8711

Authors

Zhu, Fangzhou
Padmanabhan, Nikhil
White, Martin
et al.

Publication Date

2016-09-21

DOI

10.1093/mnras/stw1515

Peer reviewed

Monthly Notices
of the
ROYAL ASTRONOMICAL SOCIETY

MNRAS **461,** 2867–2878 (2016)
Advance Access publication 2016 June 26

doi:10.1093/mnras/stw1515

Redshift weights for baryon acoustic oscillations: application to mock galaxy catalogues

Fangzhou Zhu,[1]★ Nikhil Padmanabhan,[1] Martin White,[2] Ashley J. Ross[3] and Gongbo Zhao[4,5]

[1]*Department of Physics, Yale University, New Haven, CT 06511, USA*
[2]*Department of Physics and Astronomy, U.C. Berkeley, Berkeley, CA*
[3]*Department of Physics, Center for Cosmology and Astroparticle Physics, The Ohio State University, OH 43210, USA*
[4]*National Astronomy Observatories, Chinese Academy of Science, Beijing 100012, P.R.China*
[5]*Institute of Cosmology & Gravitation, University of Portsmouth, Dennis Sciama Building, Portsmouth PO1 3FX, UK*

Accepted 2016 June 20. Received 2016 June 14; in original form 2016 April 4

ABSTRACT

Large redshift surveys capable of measuring the baryon acoustic oscillation (BAO) signal have proven to be an effective way of measuring the distance–redshift relation in cosmology. Building off the work in Zhu et al., we develop a technique to directly constrain the distance–redshift relation from BAO measurements without splitting the sample into redshift bins. We apply the redshift weighting technique in Zhu et al. to the clustering of galaxies from 1000 Quick particle mesh (QPM) mock simulations after reconstruction and achieve a 0.75 per cent measurement of the angular diameter distance $D_{\rm A}$ at $z = 0.64$ and the same precision for Hubble parameter H at $z = 0.29$. These QPM mock catalogues mimic the clustering and noise level of the Baryon Oscillation Spectroscopic Survey Data Release 12 (DR12). We compress the correlation functions in the redshift direction on to a set of weighted correlation functions. These estimators give unbiased D_A and H measurements across the entire redshift range of the combined sample. We demonstrate the effectiveness of redshift weighting in improving the distance and Hubble parameter estimates. Instead of measuring at a single 'effective' redshift as in traditional analyses, we report our D_A and H measurements at all redshifts. The measured fractional error of D_A ranges from 1.53 per cent at $z = 0.2$ to 0.75 per cent at $z = 0.64$. The fractional error of H ranges from 0.75 per cent at $z = 0.29$ to 2.45 per cent at $z = 0.7$. Our measurements are consistent with a Fisher forecast to within 10–20 per cent depending on the pivot redshift. We further show the results are robust against the choice of fiducial cosmologies, galaxy bias models, and redshift–space distortions streaming parameters.

Key words: cosmological parameters – dark energy – distance scale.

1 INTRODUCTION

Baryon acoustic oscillations (BAO) are a geometrical probe of the universe via a standard ruler provided by the 'baryon acoustic scale', a characteristic scale imprinted in the distribution of galaxies (Peebles & Yu 1970; Sunyaev & Zeldovich 1970; Bond & Efstathiou 1987; Hu & Sugiyama 1996; Eisenstein & Hu 1998). Mapping the distribution of galaxies on large scales, one finds that galaxies are slightly more likely to be separated by a distance of roughly 150 Mpc. In the hot and ionized Universe at early times, photons and baryons are tightly coupled through Thomson scattering. The strong radiation pressure pushes the photon-baryon fluid outwards in a spherical sound wave. Gravity, on the other hand, provides an inward restoring force. This competition between matter and radiation gives rise to acoustic waves within the fluid. Once recombination happens, the baryons and photons quickly decouple from each other. Photons quickly stream away from the baryons to form the cosmic microwave background (CMB). The acoustic waves then 'freeze out' as the Universe becomes neutral as it expanded and cooled. Slight density enhancements at a scale set by the acoustic scale – distance an acoustic wave can travel between the time of the big bang and recombination – is magnified by gravitational interaction to seed the galaxy formation. The acoustic scale becomes a physical scale imprinted in the CMB and is measurable in the clustering of galaxies today.

Since its first detection (Cole et al. 2005; Eisenstein et al. 2005) a decade ago, BAO has been a prominent probe featured in a host of

★E-mail: fangzhou.zhu@yale.edu

galaxy redshift surveys (Blake et al. 2007; Kazin et al. 2010; Percival et al. 2010; Beutler et al. 2011; Padmanabhan et al. 2012; Anderson et al. 2014). Large surveys like Baryon Oscillation Spectroscopic Survey (BOSS; Dawson et al. 2013; Alam et al. 2015), a part of the Sloan Digital Sky Survey (SDSS; Eisenstein et al. 2011) have been pushing the measurement of the acoustic scale to even higher precision, providing tighter constraints on our cosmological models.

In current and future generations of BAO surveys, the samples cover a wide range of redshift. In traditional analyses, one improves the resolution of the distance–redshift relation measurement by splitting samples into multiple redshift bins and analyse the signals in these narrower slices. Such a splitting scheme has several disadvantages: (1) the signal-to-noise ratio is lower in each thin slice, (2) the choice of bins is often arbitrary, and (3) one loses signal across boundaries of disjoint bins.

To tackle the problems with binning outlined above, Zhu, Padmanabhan & White (2015) proposed using a set of weights to compress the information in the redshift direction on to a small number of modes. These modes are designed to efficiently constrain the distance–redshift relation parametrized in a simple generic form over the entire redshift extent of the survey. This paper applies the methods proposed in Zhu et al. (2015) to BOSS mock galaxy catalogues. Our goal here is to demonstrate the practicability, robustness and efficiency of the method.

The paper is structured as follows. Section 2 introduces the redshift weights and covers the basics of correlation function multipoles. Section 3 describes the simulations used in this work. In Section 4, we describe the redshift weighting algorithm in detail and provide the fitting model. We discuss the improvement in the fitting of the BAO feature in Section 5. We conclude in Section 6 with a discussion of our results.

2 THEORY

2.1 Distance–redshift relation

In BAO analyses, one typically assumes a fiducial cosmology to convert the galaxy angular positions and redshifts into 3D positions and parametrizes deviations from this fiducial cosmology. We follow the parametrization proposed in Zhu et al. (2015). We denote the comoving radial distance by $\chi(z)$. Choosing a pivot redshift z_0 within redshift range of the survey, we express the ratio of the true and fiducial radial comoving distance $\chi(z)/\chi_f(z)$ as a Taylor series in $x(z) \equiv \chi_f(z)/\chi_f(z_0) - 1$,

$$\frac{\chi\,(z)}{\chi_f\,(z)} = \alpha_0 \left(1 + \alpha_1 x + \frac{1}{2}\alpha_2 x^2\right). \tag{1}$$

When the fiducial cosmology matches the true cosmology, one will measure $\alpha_0 = 1$, $\alpha_1 = 0$, and $\alpha_2 = 0$.

We can very easily extend this Taylor series to higher orders, but the order chosen here is sufficient for wide deviations in the distance–redshift relation (Zhu et al. 2015). We will discuss selecting the appropriate number of parameters later in the paper. The ratio between the fiducial and true Hubble parameter $H = 1/\chi'(z)$ is given by

$$\frac{H_f(z)}{H(z)} = \alpha_0 \left[1 + \alpha_1 + (2\alpha_1 + \alpha_2)x + \frac{3}{2}\alpha_2 x^2\right]. \tag{2}$$

The parameters α_0, α_1 and α_2 can be related to the true distance–redshift relation as

$$\alpha_0 = \frac{\chi_0}{\chi_{f,0}} \tag{3}$$

$$\alpha_1 = \frac{H_{f,0}\chi_{f,0}}{H_0\chi_0} - 1 \tag{4}$$

$$\alpha_2 = (1+\alpha_1)\chi_{f,0}[H'_{f,0} - \alpha_0(1+\alpha_1)H'_0] - 2\alpha_1. \tag{5}$$

Measuring α_0, α_1 and α_2 allows one to reconstruct the distance–redshift relation according to equation (1).

We may relate this parametrization to the (α, ϵ) parametrization [or equivalently, $(\alpha_\perp, \alpha_\parallel)$] that have been used in recent BAO analyses (Padmanabhan & White 2008; Anderson et al. 2014). In Padmanabhan & White (2008), the separation vectors between pairs of galaxies are parametrized by an isotropic dilation $\alpha(z)$ and an anisotropic warping $\epsilon(z)$ parameter. The deformation of the separation vector due to an incorrect distance–redshift relation can be parametrized as

$$r_\parallel = \alpha(1+\epsilon)^2 r^{\rm f}_\parallel \tag{6}$$

$$r_\perp = \alpha(1+\epsilon)^{-1} r^{\rm f}_\perp, \tag{7}$$

where the superscript 'f' labels the fiducial values. In the plane parallel limit, $r_\parallel = c\Delta z/H(z)$ and $r_\perp = \chi(z)\Delta\theta$. Here, Δz is the difference in redshifts of the two galaxies and $\Delta\theta$ is the angle measured by the observer of the radial direction to each galaxy,

$$\alpha(z) = \left[\frac{H_f(z)\chi^2(z)}{H(z)\chi_f^2(z)}\right]^{1/3} \tag{8}$$

$$\epsilon(z) = \left[\frac{H_f(z)\chi_f(z)}{H(z)\chi(z)}\right]^{1/3} - 1. \tag{9}$$

Together with equations (1) and (2), we can relate $\alpha(z)$ and $\epsilon(z)$ to $(\alpha_0, \alpha_1, \alpha_2)$. Working to linear order in α_1 and α_2,

$$\alpha(z) = \alpha_0 \left[1 + \frac{1}{3}\alpha_1 + \frac{1}{3}(4\alpha_1 + \alpha_2)x + \frac{5}{6}\alpha_2 x^2\right] \tag{10}$$

$$\epsilon(z) = \frac{1}{3}\alpha_1 + \frac{1}{3}(\alpha_1 + \alpha_2)x + \frac{1}{3}\alpha_2 x^2. \tag{11}$$

We discuss how these parameters shift and distort the galaxy correlation functions in Section 4.2 below.

2.2 Fitting the correlation function

As in previous BAO analyses (Anderson et al. 2014), we fit the galaxy correlation function with a template. We describe this template below and discuss how it gets distorted due to a misestimate of cosmology.

In Fourier space, we use the following template for the 2D nonlinear power spectrum (Xu et al. 2013; Anderson et al. 2014)

$$P_t\,(k,\mu) = \left(1 + \beta\mu^2\right)^2 F\,(k,\mu,\Sigma_{\rm s})\,P_{\rm dw}\,(k,\mu)\,. \tag{12}$$

The $(1 + \beta\mu^2)^2$ term represents the Kaiser effect (Kaiser 1987) with $\beta = f/b$ where $f \approx \Omega_{\rm m}(z)^{0.55}$ (Carroll, Press & Turner 1992) is the growth rate of structure and b is the large-scale galaxy bias. On small scales, the large random velocities in inner virialized clusters causes an elongation in the observed structure along the line-of-sight direction. This is known as the Finger-of-God (FoG) effect and we model in Fourier space by the multiplicative factor $F(k, \mu, \Sigma_{\rm s})$ which takes the form

$$F\,(k,\mu,\Sigma_{\rm s}) = \frac{1}{\left(1 + k^2\mu^2\Sigma_{\rm s}^2\right)^2}, \tag{13}$$

where Σ_s is the streaming scale associated with the dispersion within clusters due to random peculiar velocities.

We model the degradation of the BAO due to non-linear structure growth by a Gaussian damping term. The damping is anisotropic due to redshift space distortions (RSD). The parallel and perpendicular streaming scales $\Sigma_\parallel$ and $\Sigma_\perp$ determine the amount of damping along and perpendicular to the line of sight. The two streaming scales are related by $\Sigma_\parallel = (1+f)\Sigma_\perp$ where f is the growth rate of structure. The de-wiggled power spectrum $P_{\rm dw}(k,\,\mu)$ (Eisenstein, Seo & White 2007) is given by

$$P_{\rm dw}\,(k,\,\mu) = [P_{\rm lin}(k) - P_{\rm nw}(k)] \exp\left[-\frac{k_\parallel^2\Sigma_\parallel^2 + k_\perp^2\Sigma_\perp^2}{2}\right] + P_{\rm nw}\,(k)\,, \tag{14}$$

where $P_{\rm lin}(k)$ is the linear power spectrum from CAMB (Lewis, Challinor & Lasenby 2000). The no-wiggle spectrum $P_{\rm nw}(k)$ is the smoothed power spectrum (Eisenstein & Hu 1998) with the baryonic wiggles taken out.

For our analyses, in pre-reconstruction fits, we fix $\Sigma_s = 2\ h^{-1}$ Mpc, $\Sigma_\perp = 6\ h^{-1}$ Mpc and $\Sigma_\parallel = 9.6\ h^{-1}$ Mpc. For post-reconstruction, we use $\Sigma_s = 0\ h^{-1}$ Mpc, $\Sigma_\perp = \Sigma_\parallel = 4.3\ h^{-1}$ Mpc. These prescribed parameters are motivated by fitting to the average mock correlation function of the mocks we use. Before reconstruction, the difference in the streaming parameters $\Sigma_\perp$ and $\Sigma_\parallel$ come from the Kaiser effect. Reconstruction is expected to remove the Kaiser squashing, and hence our choice of $\Sigma_\parallel = \Sigma_\perp$ after reconstruction. In the fits to the average correlation function, the streaming parameter Σ_s is not well constrained. However, we have checked that fitting the BAO feature in individual mocks is insensitive to the choice of these streaming parameters around our prescribed values.

The multipole moments of the template power spectrum can be computed as

$$P_{\ell,t}(k) = \frac{2\ell+1}{2}\int_{-1}^{1} P_t\,(k,\,\mu)\,L_\ell(\mu)\,{\rm d}\mu, \tag{15}$$

where L_ℓ is the Legendre polynomial of order ℓ. To calculate the correlation functions, we Fourier transform the power spectrum as

$$\xi_{\ell,t}(r) = i^\ell \int \frac{k^3 {\rm d}\log k}{2\pi^2} P_{\ell,t}(k)\, j_\ell(kr). \tag{16}$$

Now we review how a misestimate of the cosmology distorts the correlation function. A perturbative expression is given by equation 26 and 27 in Xu et al. (2013). However, we use a different approach here. With equations (6) and (7), we can express the true galaxy separation and the cosine of the angle between the separation vector and line of sight in terms of the fiducial values by using α and ϵ. Given

$$r = \sqrt{r_\parallel^2 + r_\perp^2}, \tag{17}$$

$$\mu = \cos\left[\arctan\left(\frac{r_\perp}{r_\parallel}\right)\right], \tag{18}$$

we get

$$r = \alpha r^{\rm f}\sqrt{(1+\epsilon)^4(\mu^{\rm f})^2 + (1+\epsilon)^{-2}[1-(\mu^{\rm f})^2]} \tag{19}$$

$$\mu = \cos[\arctan[(1+\epsilon)^{-3}\tan(\arccos\mu^{\rm f})]]. \tag{20}$$

These are the 'true' separation and line-of-sight angle that go into the true correlation function, which can be decomposed into multipole moments using the Legendre polynomials

$$\xi_t(r,\,\mu) = \sum_\ell \xi_{\ell,t}(r) L_\ell(\mu), \tag{21}$$

where we ignore the contributions from $\ell = 10$ or higher. We find the expansion to be quickly converging and the amplitudes of higher order multipoles are significantly reduced. A non-linear model for $\xi_{\ell,\,t}(r)$ is given in the next subsection.

Substituting r and μ with the expressions above, we reach the model correlation function $\xi(r^{\rm f},\,\mu^{\rm f},\,\alpha,\,\epsilon)$. This model correlation function includes the 'isotropic dilation' and 'anisotropic warping' due to incorrectly assuming a fiducial cosmology. We then re-project on to Legendre polynomials

$$\xi_{\ell,m}(r,\,z) = \frac{2\ell+1}{2}\int_{-1}^{1} \xi(r^{\rm f},\,\mu^{\rm f},\,\alpha,\,\epsilon) L_\ell(\mu^{\rm f})\,{\rm d}\mu^{\rm f}. \tag{22}$$

This is our template for matter correlation function within a redshift slice.

2.3 Redshift weights

We define weights to compress the information in the redshift direction on to a small number of 'weighted correlation functions'. The weights are designed to optimally extract the constraints on α_0, α_1, α_2. We refer the reader to Zhu et al. (2015) for the derivation of the weights which are modelled on Tegmark, Taylor & Heavens (1997). The weights constructed for the distance–redshift parametrization in Section 2.1 are given by a multiplicative quantity $w_{\ell,i}\,{\rm d}\mathcal{W}$. Here, ${\rm d}\mathcal{W}(z)$ is given by

$${\rm d}\mathcal{W}(z) = \left(\frac{\bar{n}}{\bar{n}P+1}\right)^2 {\rm d}V(z), \tag{23}$$

where the volume of the slice is given by

$${\rm d}V(z) = \frac{\chi_f^2(z)}{H_f(z)}{\rm d}z\,{\rm d}\Omega. \tag{24}$$

$d\mathcal{W}(z)$ is the inverse of the variance of the correlation function bin at redshift z. We assume that different redshift bins are independent, so that the covariance matrix across redshifts is diagonal. In the equation above, P is the power at the BAO peak scale, and is specified to be $10^4\ h^{-3}$ Mpc^3.

The additional weights $w_{\ell,\,i}$ are given by

$$w_{0,\alpha_0} = 1 \qquad w_{2,\alpha_0} = 0 \tag{25}$$

$$w_{0,\alpha_1} = \frac{1}{3}(1+4x) \qquad w_{2,\alpha_1} = \frac{1}{3}(1+x) \tag{26}$$

$$w_{0,\alpha_2} = \frac{1}{6}(2x+5x^2) \qquad w_{2,\alpha_2} = \frac{1}{3}(x+x^2). \tag{27}$$

The first indices $\ell = 0,\,2$ indicate the weights are for fitting the monopole or quadrupole moments of the correlation function. The second indices α_i indicate the parameter one is focusing on.

3 SIMULATIONS

We test our algorithm on mock galaxy catalogues created by using the 'quick particle mesh' (QPM) method (White, Tinker & McBride 2014). These catalogues are constructed to simulate the clustering and noise level of the SDSS DR12 combined samples. For details of BOSS survey design, we refer the reader to Eisenstein et al. (2011) and Dawson et al. (2013). The mock catalogues are based on 1000 low force- and mass-resolution particle-mesh N-body simulations. Each uses 1280^3 particles in a box of side length $2560\,h^{-1}$Mpc. The simulations assume a flat Λ cold dark matter cosmology, with cosmological parameters as : $\Omega_{\rm m} = 0.29$, $\Omega_{\rm b}h^2 = 0.022\,47$, $h = 0.7$, $n_{\rm s} = 0.97$, and $\sigma_8 = 0.8$. These mocks are constructed from 1000

QPM realizations, each of which starts at $z = 25$ using second-order Lagrangian perturbation theory. The catalogues span the redshift range of $z = 0.2$–0.7 and cover both the northern and southern Galactic cap of the BOSS footprint. The QPM mocks are from a single redshift snapshot output. The mocks are populated using a bias model inferred from fitting the monopole between 20 and $50\,h^{-1}$Mpc. The mocks possess a redshift dependent galaxy bias reflecting changes in the galaxy population over the BOSS redshift range. The mocks include the effects of the angular veto mask of the BOSS galaxies, as well as an approximation to fibre collisions. The redshift selection function $n(z)$ was matched to the angular density of the DR12 sample, to make it independent of cosmology.

4 ANALYSIS

4.1 Computing the weighted correlation functions

We analyse the simulations similar to previous BOSS analyses (Anderson et al. 2014). We refer the reader to those papers for more detailed descriptions, restricting our discussion to the new aspects. The first of these is that we treat the entire BOSS redshift range as a unified sample (from $z = 0.2$ to 0.7) and do not split into smaller redshift bins. Since the efficacy of the BAO reconstruction procedure has now been well established and our redshift weights are agnostic to reconstruction, our default results will all be post-reconstruction. Our implementation of reconstruction is identical to what has been used for the SDSS and BOSS analyses (Anderson et al. 2014).

In order to compute the weighted correlation functions, we use a modified version of the Landy–Szalay estimator (Landy & Szalay 1993). As is traditional, we weight every galaxy/random by the FKP weight

$$w_{\rm FKP} = \frac{1}{1 + \bar{n}(z)P(k_0)}, \tag{28}$$

where $\bar{n}(z)$ is the number density at z, the redshift of the object. $P(k_0) = 10^4 h^{-3}{\rm Mpc}^3$ is the approximate power at the BAO scale.

We also weight each pair of galaxies/randoms by $w = 1, x, x^2$ to construct the weighted correlation functions ξ_1, ξ_x and ξ_{x^2}. Since the redshift separation between a pair that contributes to the correlation function is small, we simply use the mean redshift of each pair to compute x. The weighted 2D correlation functions are then given by

$$\xi_w^{\rm data}(r,\mu) = \frac{\widetilde{DD}(r,\mu) - 2\widetilde{DR}(r,\mu) + \widetilde{RR}(r,\mu)}{RR(r,\mu)}, \tag{29}$$

where $\widetilde{DD}$, $\widetilde{DR}$ and $\widetilde{RR}$ include the additional pair weight, whereas RR in the denominator does not. After reconstruction, this gets modified to

$$\xi_w^{\rm data}(r,\mu) = \frac{\widetilde{DD}(r,\mu) - 2\widetilde{DS}(r,\mu) + \widetilde{SS}(r,\mu)}{RR(r,\mu)}, \tag{30}$$

where S represents the shifted random particles.

In computing the pair sums, we bin the weighted pair sums in both r and μ. The r bins used here are from 0 to 200 with $4\,h^{-1}$Mpc bins. The μ bins are from 0 to 1 with 0.01 in width. From the 2D correlation function, one can compute the monopole and quadrupole moments as

$$\xi_{\ell,w}^{\rm data}(r) = \frac{2\ell+1}{2}\int_{-1}^{1} \xi_w^{\rm data}(r,\mu) L_\ell(\mu)\,{\rm d}\mu, \tag{31}$$

where L_ℓ is the Legendre polynomial of order ℓ.

We bin our estimators accordingly to the $4\,h^{-1}$Mpc resolution,

$$\xi_\ell(r_{\rm cen}) = \frac{3}{r_2^3 - r_1^3}\int_{r_1}^{r_2} r^2 \xi_\ell(r)\,{\rm d}r \tag{32}$$

gives the binned correlation function. The bin is centred at $r_{\rm cen}$, with a lower bound r_1 and an upper bound r_2.

4.2 Weighted correlation function estimators

We construct models of the monopoles and quadrupoles of the unweighted and weighted correlation functions. Since the additional weights $w_{\ell,i}$ all take the simple form of linear combinations of 1, x, and x^2, it is convenient to calculate correlation functions weighted by them instead of the original weights. Using these weights, the weighted correlation function estimators can be constructed as weighted integrals,

$$\xi_{\ell,1}(r) = \frac{1}{N}\int {\rm d}\mathcal{W}(z) b^2(z) \xi_{\ell,m}(r,z) \tag{33}$$

$$\xi_{\ell,x}(r) = \frac{1}{N}\int {\rm d}\mathcal{W}(z) x(z) b^2(z) \xi_{\ell,m}(r,z) \tag{34}$$

$$\xi_{\ell,x^2}(r) = \frac{1}{N}\int {\rm d}\mathcal{W}(z) x^2(z) b^2(z) \xi_{\ell,m}(r,z), \tag{35}$$

where $N = \int {\rm d}\mathcal{W}$ is a convenient choice of normalization and $b(z)$ is the galaxy bias. We assume that the bias is inferred from small-scale clustering measurements. We demonstrate that our results are robust to small changes in input form of $b(z)$. The above integrals are understood to be over the redshift range of the survey.

It is more efficient to compute the weighted integrals as summations across redshifts. To do this, we bin the redshift range of the combined sample [0.2, 0.7] into 50 thinner slices of width $\Delta z = 0.01$. We use the central redshift of each slice to label these slices. In each redshift bin, with the given parameters α_0, α_1, and α_2, one calculates $\chi(z)/\chi_f(z)$ and $H_f(z)/H(z)$ according to equations (1) and (2). Using the obtained χ and H ratios in equations 8 and (9), one calculates the 'isotropic dilation' parameter $\alpha(z)$ and 'anisotropic warping' parameter $\epsilon(z)$ at different redshifts. Alternatively, one can directly use equations (10) and (11) to get $\alpha(z)$ and $\epsilon(z)$. This feature is distinct from traditional analyses in which α and ϵ are only measured at the 'effective' redshift of the sample.

For efficient calculation of the redshift dependent $\xi_{\ell,m}(r,z)$, we pre-compute and tabulate correlation function monopoles and quadrupoles by fixing $\alpha = 1$ while ϵ ranges from -0.2 to 0.2 with intervals of 0.001. We first calculate the correlation function by interpolating in the ϵ direction. This gives us the correlation function corresponding to $\alpha = 1$ and $\epsilon = \epsilon(z)$. We then interpolate the obtained correlation function at separation scale $\alpha(z)r$.

Within each slice, we also calculate the inverse variance factor $\Delta\mathcal{W}(z)$ and the additional weights $x(z)$ as they will be used to weight the correlation functions in different slices. In calculating $\Delta\mathcal{W}(z)$ using equation (23), the volume of each slice is calculated as

$$\Delta V(z) \propto \frac{\chi_f^2(z)}{H_f(z)}\Delta z. \tag{36}$$

Once all these ingredients are in hand, we weight the correlation function monopoles and quadrupoles by $\Delta\mathcal{W}(z)w_z$, where $w_z = 1, x, x^2$ and sum across redshifts. We thus achieve the 'unweighted', 'x-weighted', and 'x^2-weighted' monopole and quadrupole estimators.

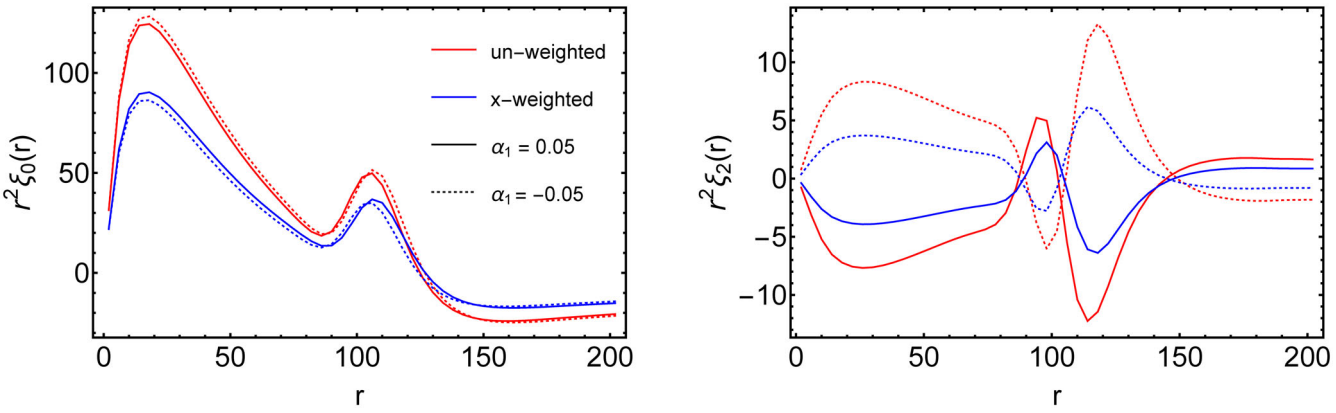

Figure 1. The model monopole (left-hand panel) and quadrupole (right-hand panel) with a varying α_1. The red lines plot the unweighted monopoles and quadrupoles while the blue lines are for the x-weighted. The solid lines correspond to $\alpha = 0.05$ while the dotted lines are for $\alpha = -0.05$. For plotting convenience, we have multiplied the x-weighted monopoles and quadrupoles by a factor of -5. All curves assume a pivot redshift of $z_0 = 0.57$ and fiducial model parameters $\Sigma_\perp = \Sigma_\parallel = 4.3\,h^{-1}$Mpc with $\beta = 0$ (the centre of the prior in our post-reconstruction fits). In monopole, α_1 works to change the position of unweighted and x-weighted BAO features in opposite directions. The quadrupole changes sign when we switch α_1 from 0.05 to -0.05. The crest-trough feature at the BAO scale seen in the unweighted and x-weighted quadrupoles move in opposite directions with varying α_1 analogous to the monopoles.

Fig. 1 shows variations of the expected correlation function monopole and quadrupole with α_1 while holding $\alpha_0 = 1$ fixed. We have assumed a flat cosmology with $\Omega_m = 0.29$, $\Omega_b h^2 = 0.022\,47$, $h = 0.7$, $n_s = 0.97$, and $\sigma_8 = 0.8$ (the QPM cosmology described in Section 3). In Fourier space, this model is given by the de-wiggled power spectrum as below in equation (14). One can see from the monopole (left-hand panel) that α_1 causes shift of the unweighted and x-weighed monopole BAO peaks in opposite directions. In contrast, since α_0 causes isotropic shifts, it shifts the BAO peak in the unweighted and x-weighted monopoles in the same direction. The quadrupoles (right-hand panel) encode the anisotropic signal. Since Fig. 1 assumes isotropic damping $\Sigma_\perp = \Sigma_\parallel = 4.3\,h^{-1}$Mpc, the only anisotropic signal (quadrupole) comes from the misestimation of the distance–redshift relation characterized by α_1. We see that the quadrupoles become inverted when we switch from $\alpha_1 = 0.05$ to -0.05. On top of the sign change, the BAO feature (the crest-trough at the acoustic scale) in the unweighted and x-weighted quadrupoles shift in opposite directions analogous to the monopoles.

4.3 Fitting the acoustic feature

The fitting aims to minimize the χ^2 goodness-of-fit indicator given by

$$\chi^2 = (\boldsymbol{m} - \boldsymbol{d})^T C^{-1} (\boldsymbol{m} - \boldsymbol{d}). \tag{37}$$

We describe the data vector $\boldsymbol{d}$, the model vector $\boldsymbol{m}$, and the covariance matrix C below.

We perform two sets of fits on the mock correlation functions with the model outlined in the previous sections. In the first set of fits, we fit the 'unweighted' correlation functions. We will call this set of fits 'unweighted fits' or '1 fits'. In the second set, we simultaneously fit the unweighted and the x-weighted correlation functions. We will call this set 'weighted fits' or '1+x fits'.

We adopt $48\,h^{-1}$Mpc $< r < 152\,h^{-1}$Mpc as our fiducial fitting range with $4\,h^{-1}$Mpc bins. We use the bin centre to label each bin. The monopole and quadrupole data vector $\boldsymbol{d}_{\ell,w}$ corresponds to 26 points each, with $50\,h^{-1}$Mpc being the first bin and $150\,h^{-1}$Mpc the last one.

For 'unweighted' fits, we simultaneously fit the unweighted monopole and quadrupole correlation function $\boldsymbol{d}_{0,1}$ and $\boldsymbol{d}_{2,1}$. The data vector and model vector take the form

$$\boldsymbol{d} = \begin{pmatrix} \boldsymbol{d}_{0,1} \\ \boldsymbol{d}_{2,1} \end{pmatrix} \qquad \boldsymbol{m} = \begin{pmatrix} \boldsymbol{m}_{0,1} \\ \boldsymbol{m}_{2,1} \end{pmatrix}. \tag{38}$$

The monopole/quadrupole are denoted by $\ell = 0$, 2 respectively, while $w = 1$, x indicate the z-weight.

For the 'weighted' fits ('1+x'), we simultaneously fit the unweighted and x-weighted monopoles and quadrupoles. The data vector and model vector take the form

$$\boldsymbol{d} = \begin{pmatrix} \boldsymbol{d}_{0,1} \\ \boldsymbol{d}_{2,1} \\ \boldsymbol{d}_{0,x} \\ \boldsymbol{d}_{2,x} \end{pmatrix} \qquad \boldsymbol{m} = \begin{pmatrix} \boldsymbol{m}_{0,1} \\ \boldsymbol{m}_{2,1} \\ \boldsymbol{m}_{0,x} \\ \boldsymbol{m}_{2,x} \end{pmatrix}. \tag{39}$$

The data vectors $\boldsymbol{d}_{\ell,w}$ are given by $\xi^{\rm data}_{\ell,w}(r)$ in equation (31). The model vectors $\boldsymbol{m}_{\ell,w}$ will be explained in detail in the next subsection. Once again, in the combined column vector $\boldsymbol{d}$ and $\boldsymbol{m}$, each vector $\boldsymbol{d}_{\ell,w}$ and $\boldsymbol{m}_{\ell,w}$ corresponds to 26 points.

4.3.1 *The fiducial fitting model*

We fit our correlation functions to

$$\xi^{\rm fit}_{\ell,w}(r) = B_w^2 \xi_{\ell,w}(r) + A_{\ell,w}(r), \tag{40}$$

where $\xi_{\ell,w}(r)$ is the weighted correlation function while $A(r)$ absorbs unmodelled broad-band features including RSD and scale-dependent bias following Anderson et al. (2014). We assume

$$A_{\ell,w}(r) = \frac{a_{\ell,w,1}}{r^2} + \frac{a_{\ell,w,2}}{r} + a_{\ell,w,3}. \tag{41}$$

We allow a multiplicative factor $B_w^2 \sim 1$ to vary in order to adjust the amplitudes of the correlation functions. Note that B_w^2 determines the amplitudes of the monopole and quadrupole together while β sets the relative amplitude between the two.

4.3.2 Covariance matrices

The most direct way to calculate the covariance matrix is from the mock catalogues. The (i, j) element of the covariance matrix is calculated as

$$C_{ij} = \frac{1}{N_s - 1} \sum_{n=1}^{N_s} \left[d_n(r_i) - \bar{d}(r_i) \right] \left[d_n(r_j) - \bar{d}(r_j) \right], \quad (42)$$

where N_s is the total number of mocks, $d_n(r)$ is the correlation function calculated from the nth mock and $\bar{d}(r)$ is the average of the mock correlation functions.

When estimating the inverse covariance matrix, Ψ, from mocks, we account for the bias from the asymmetry of the Wishart distribution by multiplying the inverse covariance matrix by a pre-factor $(1 - D)$, namely, $\Psi = (1 - D)C^{-1}$ (Hartlap, Simon & Schneider 2007; Percival et al. 2014) where

$$D = \frac{N_b + 1}{N_s - 1}. \quad (43)$$

Here, N_b is the size of the data vector.

This correction is also important in calculating the expected χ^2 value. If one is fitting a sample by using the covariance matrix calculated from the same sample, the expected χ^2 is equal to the degree-of-freedom multiplied by the pre-factor $(1 - D)$. We refer the reader to the appendix for a derivation of this relation.

4.3.3 Summary of parameters

In the unweighted fits, the non-linear parameters we fit for are B_1^2, β, α_0, and α_1, in addition to the $2 \times 3 = 6$ linear nuisance parameters in $A_{\ell,w}(r)$, a total of 10 parameters. Note that $\ell = 0$, 2 and $w = 1$, yielding a data vector with 52 elements, and a fit with 42 degrees of freedom. We calculate the expected χ^2 for individual mocks by including the pre-factor described in Section 4.3.2, and get the expected χ^2 to be 40.

Similarly, in the weighted fits, the non-linear parameters we fit for are B_1^2, B_x^2, β, α_0, and α_1, in addition to the $4 \times 3 = 12$ linear nuisance parameters in $A_{\ell,w}(r)$ where $w = 1$ or x. This gives a total of 17 parameters of interest. Therefore, dof $= 4 \times 26 - 17 = 87$ in the weighted fit. This yields the expected χ^2 to be 78.

We obtain the set of best-fitting model parameters by minimizing χ^2 as in equation (37). The non-linear parameters are handled through a simplex algorithm (Nelder & Mead 1965) while the linear nuisance parameters are obtained using a least-squares method nested within the simplex. For each set of non-linear parameters, the least-squares algorithm gives the corresponding best-fitting linear parameters. The simplex algorithm then searches the non-linear parameter space until the best-fitting parameters that minimize χ^2 are achieved.

Some mocks possess a weak BAO feature. The low signal to noise causes the nuisance polynomial to become the dominant contribution to the model correlation function. To avoid these undesirable cases, we adopt a Gaussian prior for β centred around 0.35 with standard deviation 0.15. After reconstruction, we put a Gaussian prior of the same width centred around 0 as reconstruction partially removes the Kaiser effect.

In the default fits, we allow α_0 and α_1 to float while fixing $\alpha_2 = 0$. We discuss extending our fits to include α_2 in Section 5.2.4 below.

5 RESULTS

5.1 Fiducial results

We present the results of the fits to the QPM mock correlation functions using both the 'unweighted' and the 'weighted' fits. The fits assume the QPM cosmology as the fiducial cosmology and assume a pivot redshift $z_0 = 0.57$. We will then compare the results from 'unweighted' and 'weighted' fits and comment on the effectiveness of redshift weighting in measuring the distance–redshift relation and the Hubble parameter to a higher accuracy.

We plot the average monopole and quadrupole of 1000 mocks before and after reconstruction in Fig. 2. The bands contain the error for individual mocks. One can see that the 'x-weighted' monopoles and quadrupoles are inverted as compared to the 'unweighted' ones. The inversion comes from an overall negative weight. Albeit inverted, the acoustic feature is clearly visible in the 'x-weighted' monopoles. A comparison of the monopoles before and after reconstruction shows that the acoustic peak in the monopole is more pronounced after reconstruction, suggesting reconstruction is effective in partially undoing the damping of the BAO feature due to non-linear evolution. Motivated by a fit to the average correlation function, we have chosen $\Sigma_\perp = 6\,h^{-1}$ Mpc and $\Sigma_\parallel = 9.6\,h^{-1}$ Mpc before reconstruction and $\Sigma_\perp = \Sigma_\parallel = 4.3\,h^{-1}$ Mpc for post-reconstruction fits. In addition, one can see the quadrupole amplitude is substantially smaller and close to zero after reconstruction on large scales. This confirms that reconstruction partially removes the effects of RSD.

We measure α_0 and α_1 for each mock using the fitting procedure and model outlined in Section 4. Since our fiducial cosmology is the same as simulation cosmology, we expect $\langle \alpha_0 \rangle = 1$ and $\langle \alpha_1 \rangle = 0$ if our estimators are unbiased. Fig. 3 shows fit to an example 'unweighted' post-reconstruction monopole and quadrupole, while Fig. 4 shows the 'weighted' fit to the same mock where we simultaneously fit the 'unweighted' and 'x-weighted' monopoles and quadrupoles.

A summary of our fitting results is in Table 1. The results are all consistent with expected values within uncertainties, suggesting our weighted correlation functions are an unbiased estimator. Furthermore, applying the z-weights significantly reduce the α_0 and α_1 errors.

Fig. 5 shows the scatter plot of α_0 and α_1 we obtain from 1000 mocks post-reconstruction. The left-hand panel is from 'unweighted' fits and the right-hand panel is after weights are being applied. We see that the two parameters are not highly correlated at this choice of the pivot redshift. We also plot the 1σ and 2σ error ellipse predicted from a Fisher matrix calculation (see Section 5.3 below) in both panels. The ellipses in the two panels are of the same size. One can see from the 'weighted' scatter plot that most of the best-fitting (α_0, α_1) points fall within the 2σ contour. This indicates that redshift weighting helps shrink the errors down towards the forecasted level.

With α_0 and α_1 in hand, we reconstruct the distance–redshift relation from equation (1). Similarly, we also reconstruct the Hubble parameter from equation (2). For each reconstructed mock, we use these best-fitting α_0 and α_1 parameters to calculate the two relations and calculate the average and the scatter of each relation. We plot the reconstructed $\chi(z)/\chi_f(z)$ and $H(z)/H_f(z)$ with 1σ error in Fig. 6. The plots show the reconstructed relations from both the 'unweighted' fits and the 'weighted' fits. Both $\chi(z)/\chi_f(z)$ and $H(z)/H_f(z)$ are centred around 1 at all redshifts, suggesting applying the redshift weights give unbiased distance and Hubble parameter

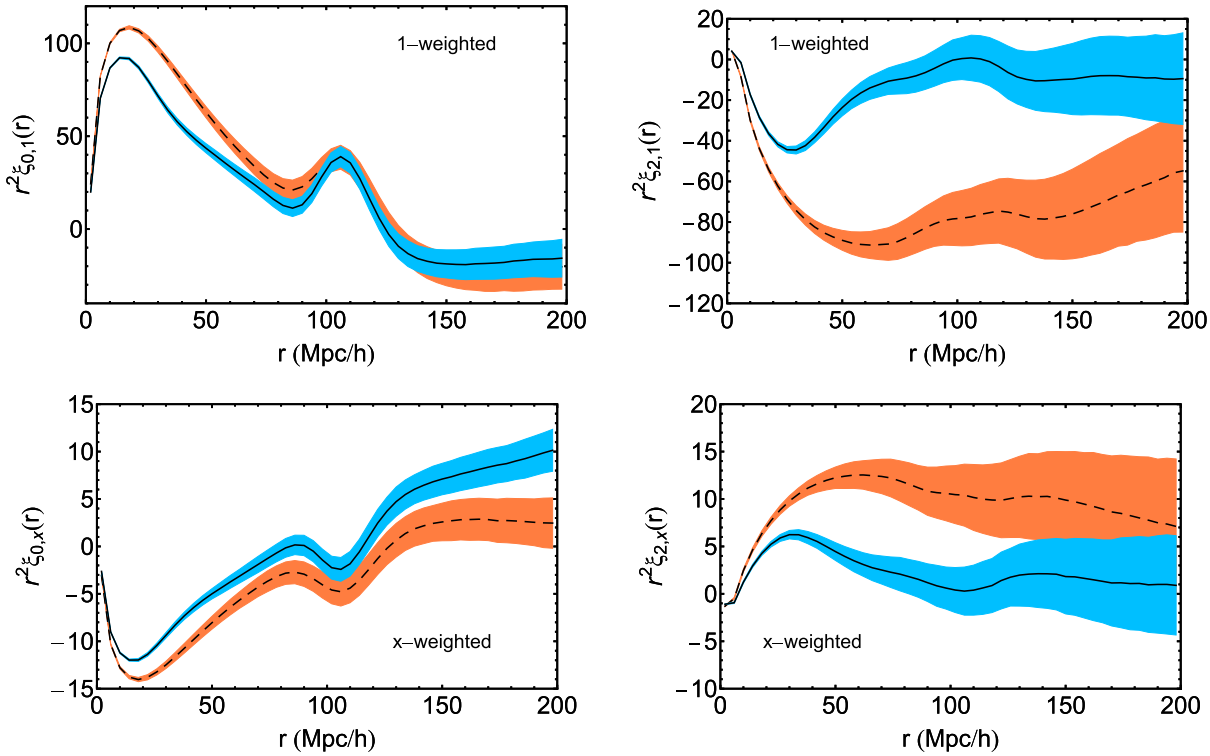

Figure 2. The average monopoles (left) and quadrupoles (right) from the 1000 QPM mocks. The error bands plotted are that of an individual mock, which are $\sqrt{1000}$ bigger than for that of the average correlation function. The dashed lines (orange bands) are pre-reconstruction mocks, while the solid lines (blue bands) correspond to post-reconstruction. The top panels show the 'unweighted' monopoles and quadrupoles while the bottom show the '*x*-weighted' ones. One can see that the '*x*-weighted' monopoles and quadrupoles are inverted as compared to the 'unweighted' ones, due to an overall negative weight. The acoustic feature is clearly visible in the '*x*-weighted' monopoles. The reconstructed monopole moments show a sharpened acoustic peak, suggesting reconstruction partially removes the degradation of BAO due to non-linear evolution. The quadrupole amplitudes are significantly reduced after reconstruction. At large scales, quadrupole moments are close to 0, indicating the efficiency of reconstruction at removing the Kaiser effect.

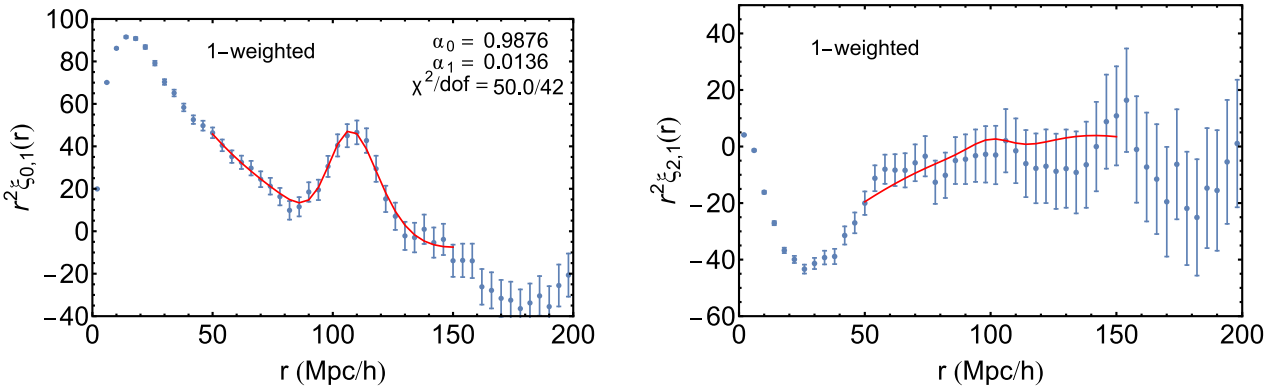

Figure 3. The best fit to a sample unweighted monopole (left) and quadrupole (right) from a reconstructed mock correlation function. The (blue) bars are monopoles and quadruples from a sample mock with 1σ error bars. The solid (red) lines are the best-fitting models. The best-fitting parameters and the corresponding χ^2 values are listed on the figure.

measurements. From the figures, we also find that weighting allows us to measure both χ and H to higher precision. The error of $\chi(z)/\chi_f(z)$ is smallest at higher redshifts. This reflects the fact that our sample is most concentrated at close to its 'effective redshift'.

5.2 Robustness of fits

The fitting results above have assumed our default choices of fiducial cosmology, RSD streaming parameters, and galaxy bias. We explore the effects of varying these below.

5.2.1 Pivot redshift

We repeat the analysis by assuming a different pivot redshift $z_0 = 0.4$. The weights are different from the set computed for $z_0 = 0.57$ since the weights are defined relative to the comoving distance at the pivot redshift.

We fit the 1000 reconstructed mocks assuming $z_0 = 0.4$ and summarize the statistics in the scatter plot in Fig. 7. The measurements are still consistent with $\langle\alpha_0\rangle = 1$ and $\langle\alpha_1\rangle = 0$ within uncertainties. This confirms that weighting yields non-biased measurements

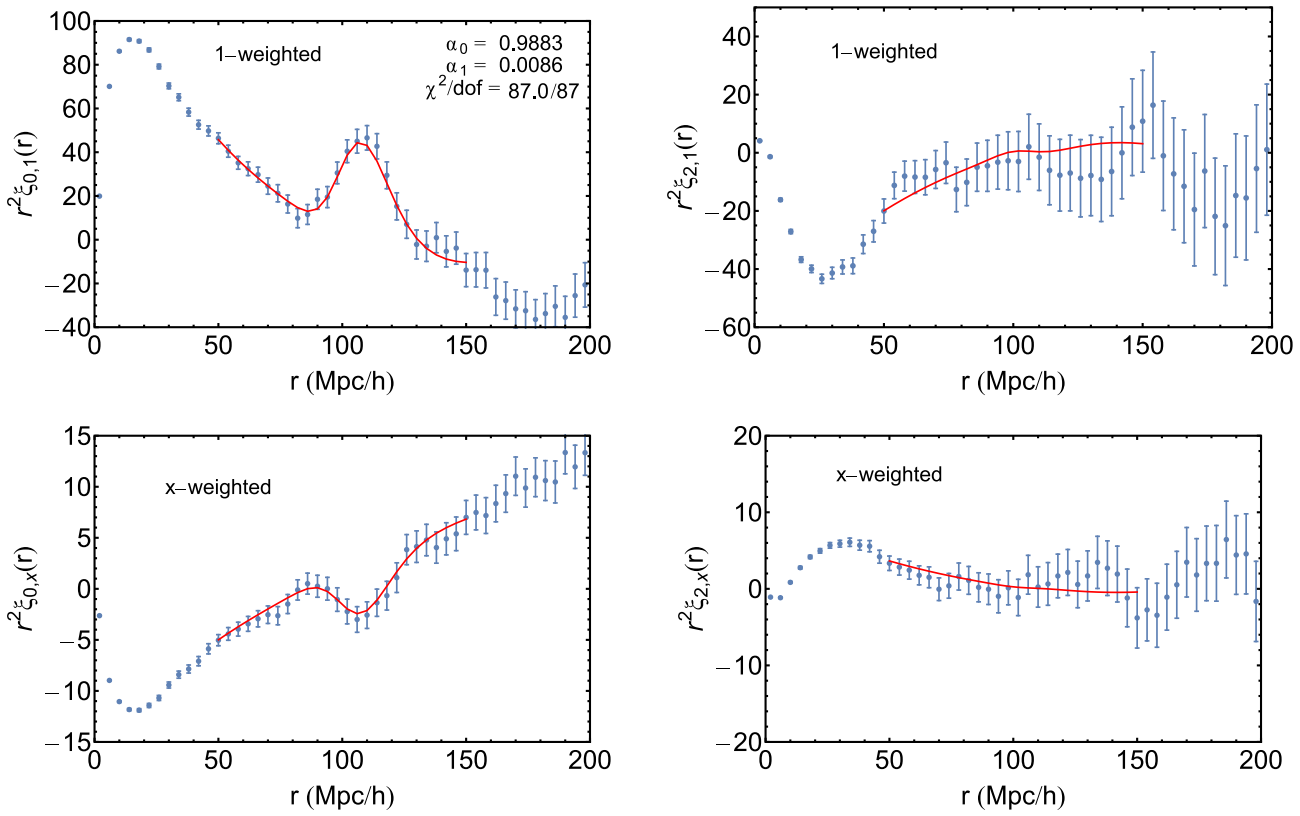

Figure 4. Sample 'weighted' fit to the unweighted and x-weighted monopoles (left) and quadrupoles (right) of the same mock as in Fig. 3. The top two panels are the unweighted monopoles and quadrupoles while the bottom two are weighted by x. The best-fitting models [solid (red) lines] are overplotted.

Table 1. Mean and standard deviations of best-fitting α_0 and α_1 from 'unweighted fits' and 'weighted fits' with various models. The model is given in column 1. The mean and standard deviation of the best-fitting parameters from the mocks are given in column 2 and 3. The mean χ^2/dof is given in column 4. For a relation between the expected average χ^2 and dof, see the appendix.

Model	α_0	α_1	$\langle\chi^2\rangle$/dof
	Before reconstruction		
Fiducial, weighted	1.0023 ± 0.0115	0.0020 ± 0.0332	78.66/87
Fiducial, unweighted	1.0022 ± 0.0118	0.0036 ± 0.0478	40.53/42
	After reconstruction		
Fiducial, weighted	1.0005 ± 0.0079	0.0025 ± 0.0205	80.00/87
Fiducial, unweighted	1.0002 ± 0.0084	0.0050 ± 0.0276	41.87/42
Fit w/ $(\Sigma_\perp, \Sigma_\parallel) \rightarrow (3, 3)\ h^{-1}$ Mpc	1.0002 ± 0.0079	0.0030 ± 0.0207	80.61/87
Fit w/ $\Sigma_s = 2\ h^{-1}$Mpc	1.0004 ± 0.0079	0.0036 ± 0.0205	80.30/87
Fit w/ constant $b(z) = 1.7$	1.0002 ± 0.0079	0.0030 ± 0.0209	80.00/87
Fit w/ $70 < r < 150\ h^{-1}$Mpc	1.0004 ± 0.0079	0.0021 ± 0.0208	61.22/67
$z_{\rm pivot} = 0.4$	1.0000 ± 0.0102	0.0015 ± 0.0135	80.01/87
Fit w/ $\Omega_m = 0.25$ cosmology, assuming $\alpha_2 = 0$	1.0603 ± 0.0084	-0.0145 ± 0.0203	80.30/87
Fit w/ $\Omega_m = 0.25$ cosmology with floating α_2 (expect $\alpha_0 = 1.0599$, $\alpha_1 = -0.0161$, and $\alpha_2 = 0.0018$)	1.0605 ± 0.0083	-0.0155 ± 0.0205	119.97/131

of both parameters. In addition, redshift weighting again demonstrated efficiency in lowering the standard deviation of α_0 and α_1. The error on α_0 is larger than the $z_0 = 0.57$ case while the error on α_1 is smaller. Furthermore, the scatter plot shows clear correlation between the two parameters at this choice of pivot redshift.

We reconstruct the distance–redshift relation and Hubble parameter based on the 'weighted' fits and compare them against the $z_0 = 0.57$ results. The comparison is summarized by Fig. 8. The analyses using two different pivot redshifts give almost identical reconstructed distance and Hubble parameter measurements.

5.2.2 *Fiducial cosmology*

We test the robustness of the fitting routine and the gain in redshift weighting by using a fiducial cosmology that is different from the QPM cosmology. We pick a flat cosmology with $\Omega_m = 0.25$. We fix

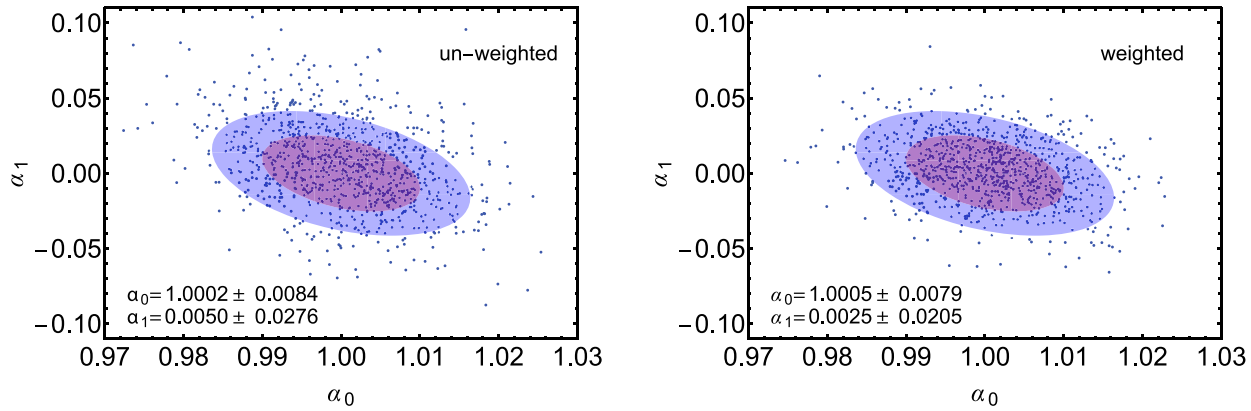

Figure 5. The best-fitting α_1 versus α_0 from the fits to 1000 individual mocks after reconstruction, assuming a pivot redshift $z_0 = 0.57$ in the analysis. The left-hand panel shows best-fitting values from the 'unweighted' fits. The right-hand panel is the same plot from 'weighted' fits. As expected, redshift weighting reduces the scatter of α_1. The red and blue contours are 1σ and 2σ contours based on a Fisher forecast.

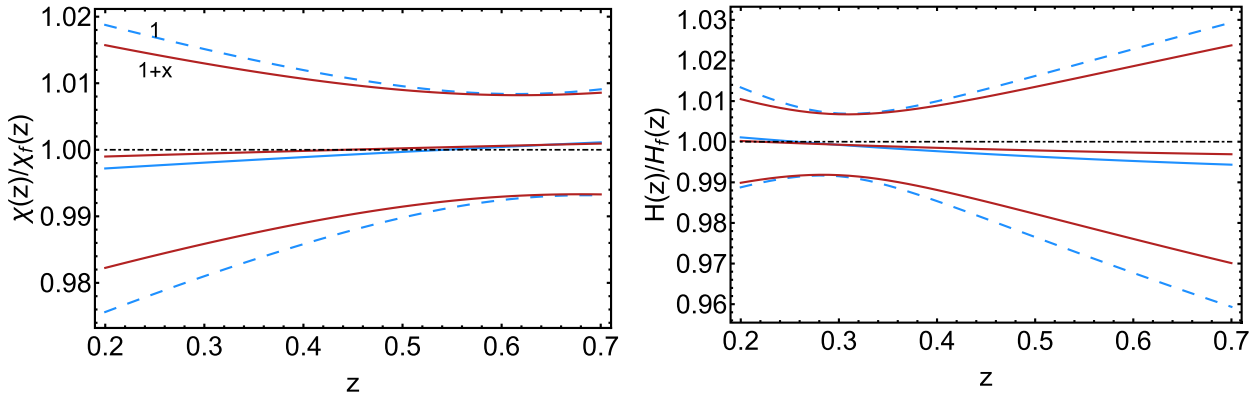

Figure 6. Distance $\chi(z)$ (left-hand panel) and $H(z)$ measurements (right-hand panel) from 1000 reconstructed mocks. Upper lines and bottom lines correspond to one standard deviation above and below the average (middle lines). The dashed (blue) line is from 'unweighted' fitting of the mocks and the solid (red) line is from 'weighted' fits where we simultaneously fit the unweighted and x-weighted correlation functions. The z-weights are effective in generating an unbiased and more accurate measurement of both the distance and Hubble parameter.

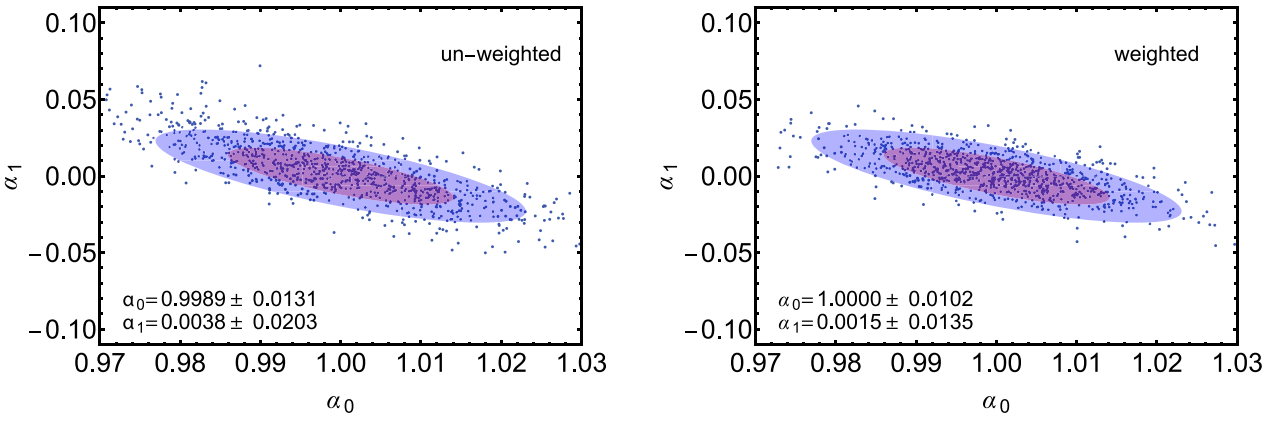

Figure 7. The same plot as Fig. 5 while assuming the pivot redshift $z_0 = 0.4$ in the analysis. The scatter plot shows the same trend as in the $z_0 = 0.57$ case that redshift weighting makes the points come closer.

$\Omega_m h^2 = 0.1421$ and $\Omega_b h^2 = 0.022\,47$ to be the same as the QPM cosmology so that the sound horizon stays the same.

Under this fiducial cosmology and pivot redshift $z_0 = 0.57$, we expect $\alpha_0 = 1.0599$ and $\alpha_1 = -0.0161$. Fitting the 1000 mocks yields $\alpha_0 = 1.0603 \pm 0.0084$ and $\alpha_1 = -0.0145 \pm 0.0203$, consistent with the expected values within uncertainties. This indicates the analysis and measurements are unbiased when the assumed fiducial cosmology differs from the true (simulation) cosmology.

5.2.3 *Galaxy bias model*

Our derivation of the redshift weights assumes a constant galaxy bias across redshifts. However, measuring the galaxy bias from

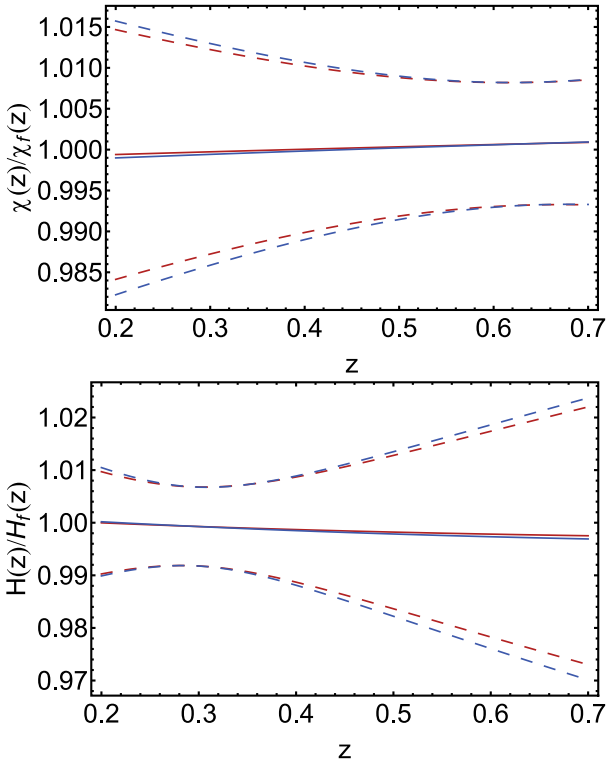

Figure 8. Comparison of $\chi(z)$ (top panel) and $H(z)$ measurements (bottom panel) under two different pivot redshifts, $z_0 = 0.57$ (blue) and $z_0 = 0.4$ (red). The fits to 1000 reconstructed mocks are done by using the 'weighted' fits. Upper lines and bottom lines correspond to one standard deviation above and below the average. We see that the reconstructed relations using two different pivot redshifts are almost identical, with the $z_0 = 0.4$ case doing slightly better.

small-scale clustering reveals a bias varying with redshift. The variation is rather mild, ranging from 1.65 to 1.8 in the redshift range $z = 0.2$–0.7. This variation not only makes the default weights not optimal, it potentially can also bias the distance and Hubble measurement. We explicitly test for the effect by re-running the fits but assuming a constant galaxy bias $b(z) = 1.7$. The results (as presented in Table 1) turn out to be almost identical to the default fits within uncertainty.

5.2.4 Including α_2

In the default fits, we have held α_2 to be fixed at 0. However, the expected a_2 does not vanish when the fiducial cosmology differs from the true (QPM in our case) cosmology. The exclusion of α_2 as a fitting parameter is equivalent to approximating the distance–redshift relation paramtrization to the first order. This approximation can potentially bias the measured α_0 and α_1, and in turn, bias the distance and Hubble parameter measurements. We explicitly test for such an effect by re-running the fits and including α_2 as a fitting parameter. The fits assume a flat fiducial cosmology with $\Omega_m = 0.25$ (as in Section 5.2.2). Under this cosmology, we expect $\alpha_0 = 1.0599$, $\alpha_1 = -0.0161$, and $\alpha_2 = 0.0018$. The fits yield $\alpha_0 = 1.0605 \pm 0.0083$, $\alpha_1 = -0.0155 \pm 0.0205$, and $\alpha_2 = -0.0175 \pm 0.1521$, all consistent with the expected theory values within uncertainty. The measured 15 per cent error on the α_2 measurements suggests it cannot be well constrained by these data. Comparing the fitting results that assume $\alpha_2 = 0$ with our α_0 and α_1 measurements that includes α_2 as a fitting parameter, we see that the former is unbiased within uncertainty. The reason is that the expected α_2 is very close to 0. This is true for other reasonable fiducial cosmologies. In addition, we reconstruct the distance–redshift relation and Hubble parameter with the full quadratic expansion in equations (1) and (2) and find the results are almost identical to assuming $\alpha_2 = 0$. Hence we claim in general the default fits with α_2 forced to be zero are sufficient and unbiased within uncertainty.

5.3 Comparison with Fisher matrix forecasts

The Fisher matrix is a commonly used tool in estimating errors from a planned survey. Inverting the Fisher matrix gives the parameter covariance matrix. It serves as a marker for the theoretical lower limit of errors measured from a planned survey. We describe the details that go into a Fisher matrix calculation and compare the errors from our 'weighted' fits to the Fisher matrix forecasts.

We break the redshift range of the survey [0.2, 0.7] into 50 bins, each with width $\Delta z = 0.01$. The volume of each slice is computed according to

$$\Delta V_z = \frac{\chi_f^2(z)}{H_f(z)} \Delta z \Delta\Omega, \tag{44}$$

where $\Delta\Omega$ is the angle covered by the BOSS DR12 area.

In each redshift slice, we calculate the Fisher matrix for $\chi(z)$ and $1/H(z)$ according to Seo & Eisenstein (2007). We assume $\beta = 0$, $\Sigma_s = 0$, and $\Sigma_\perp = \Sigma_\parallel = 4.3\,h^{-1}$Mpc post-reconstruction motivated by fits to the average correlation function.

We then rotate the basis into α_0, α_1, and α_2 through a linear transformation:

$$\mathcal{F}_{\alpha_0,\alpha_1,\alpha_2} = J^T \mathcal{F}_{\chi,H^{-1}} J, \tag{45}$$

where J is the Jacobian matrix

$$J = \begin{pmatrix} \frac{\partial\chi}{\partial\alpha_0} & \frac{\partial\chi}{\partial\alpha_1} & \frac{\partial\chi}{\partial\alpha_2} \\ \frac{\partial H^{-1}}{\partial\alpha_0} & \frac{\partial H^{-1}}{\partial\alpha_1} & \frac{\partial H^{-1}}{\partial\alpha_2} \end{pmatrix}. \tag{46}$$

If one focuses on α_0 and α_1 and have α_2 fixed to be 0, the Jacobian matrix is made up of the first two columns.

Using equations (1) and (2), we compute the Jacobian matrix as

$$J = \begin{pmatrix} \chi_f(z) & \chi_f(z)x & \frac{1}{2}\chi_f(z)x^2 \\ \frac{1}{H_f(z)} & \frac{1+2x}{H_f(z)} & \frac{x+\frac{3}{2}x^2}{H_f(z)} \end{pmatrix}. \tag{47}$$

Once we have calculated the Fisher matrix for α_0, α_1, and α_2 in each redshift slice, we combine the errors calculated in these slices through inverse variance weighting. This corresponds to a sum of the Fisher matrices

$$F = \sum_z F(z). \tag{48}$$

Inverting the total Fisher matrix gives the parameter covariance matrix $C = F^{-1}$.

Focusing on the two parameter (α_0, α_1) case, the Fisher matrix calculation for $z_0 = 0.57$ yields the estimated errors of α_0, α_1 to be 0.66 and 1.67 per cent, respectively. For the $z_0 = 0.4$ case, the Fisher forecast yields 0.93 per cent error on α_0 and 1.22 per cent on α_1. These errors are about 10–20 per cent lower than what we have measured from the weighted fits. In the three parameter (α_0, α_1, α_2) case, the errors of α_0 and α_1 remain comparable as in the two parameter case. The estimated error of α_2 is 11 per cent, suggesting α_2 cannot be well constrained by these data.

To analyse the impact from different choices of pivot redshifts, we calculate the errors on α_0 and α_1 for different pivot redshifts. We

Table 2. Variation of the estimated α_0 and α_1 errors with Hubble parameter errors increased by 2 folds, 10 folds, and 1000 folds.

H error increased by	α_0 error (in per cent)	α_1 error (in per cent)
Original	0.66	1.6
2×	0.72	2.5
10×	0.94	4.1
1000×	1.04	4.5

find that a higher pivot redshift allows a better measurement of α_0 but a worse α_1. We also find that the correlations between the two parameters $\rho_{\alpha_0\alpha_1} = C_{\alpha_0\alpha_1}/\sqrt{C_{\alpha_0\alpha_0}C_{\alpha_1\alpha_1}}$ increases from $\rho_{\alpha_0\alpha_1} = -0.9$ at $z = 0.2$ to $\rho_{\alpha_0\alpha_1} = 0.1$ at $z = 0.7$. They decorrelate at redshift $z = 0.68$. We calculate the forecasted errors of $\chi(z)/\chi_f(z)$ and $H(z)/H_f(z)$ at different pivot redshifts and found them to be insensitive to the choice of the pivot redshift. The error of $\chi(z)/\chi_f(z)$ reaches as low as 0.61 per cent at around $z = 0.68$. The error of $H(z)/H_f(z)$ is smallest at roughly $z = 0.3$. These are all consistent with the mock results within 10–20 per cent.

The Fisher matrix calculation also allows us to gain insight into the constraining power of D_A and H measurements on α_0 and α_1. We make the following experiment in our Fisher matrix calculation. In each redshift slice, we increase the error of H while keeping the error of χ the same. Table 2 lists the estimated α_0 and α_1 errors with the H errors increased by 2 fold, 10 fold, and 1000 fold in each redshift slice. When we increase the error of the Hubble parameter H by 2, we find that α_0 error goes up by 10 per cent while the α_1 error quickly worsens. This suggests the H measurement is important for constraining α_1 to high precision. As we continue to increase H errors, α_0 and α_1 errors continue to grow. The case where the H error is increased by a factor of 1000 mimics the case in which the survey only affords D_A measurements but not H. In this case, the information is predominantly from D_A measurements. The estimated error of α_0 is at the 1 per cent level and α_1 error is 4.5 per cent.

6 DISCUSSION

This paper presents the results of applying redshift weighting as proposed in Zhu et al. (2015) to BAO analyses. Different from previous BAO analyses, redshift weighting allows us to analyse a full sample without the need of splitting the sample into multiple redshift bins. We validate the method on a set of 1000 QPM mocks tailored to mimic the clustering noise level of BOSS DR 12.

We approximate the distance–redshift relation, relative to a fiducial model, by a quadratic function. By measuring the coefficients from the mocks, we then reconstruct the distance and Hubble parameter measurements from the expansion. Our approach thus gives measurements of $D_A(z)$ and $H(z)$ at all redshifts within the range of the sample. This is different from previous analyses in which only measurements at the 'effective redshift' are given. Our fits assume the Hubble parameter to be the inverse derivative of the comoving distance. We are thus jointly measuring D_A and H with this additional constraint in place. This differs from traditional analyses in which D_A and H are measured separately.

The key advantage of redshift weighting is the optimized use of the full sample. We compress the information in the redshift direction into a small number of 'weighted correlation functions'. These weighted estimators preserve nearly all the BAO information without diluting the signal-to-noise per measurement. We found that fitting these weighted estimators improves the distance and Hubble parameter measurements. Our mock results yield a 0.75 per cent D_A measurement at $z = 0.64$ and the same precision for H at $z = 0.29$. We can compare our results to the results of Cuesta et al. (2016) who analysed a similar sample by splitting into two redshift bins. In that work, they measured D_A and H with 2.5 and 5.2 uncertainty, respectively, for the LOWZ sample ($0.2 < z < 0.43$), and 1.6 and 3.1 per cent for CMASS ($0.43 < z < 0.7$).

We demonstrate that our method is unbiased and robust against the choices of fiducial cosmologies, pivot redshift, RSD streaming parameters, and galaxy bias models. We have also extended the fits to include the second-order term in the expansion of our distance–redshift parametrization and found the results to be almost identical. We thus claim the default fits with the first order of the parametrization is sufficient.

We compare our results with a Fisher matrix forecast. Our results are 10 per cent worse than the estimated Fisher errors. We experiment with the Fisher matrix calculation by degrading H measurements by 1000 fold in each redshift slice and re-estimate α_0 and α_1 uncertainties. At pivot redshift $z = 0.57$, the α_0 and α_1 errors degrade from 0.66 and 1.6 per cent to 1 and 4.5 per cent. This exercise allows us to estimate how much information D_A measurement alone affords in constraining α_0 and α_1. This estimate is potentially useful for photometric surveys.

Our algorithm and results have important implications for BAO measurements from current and future redshift surveys. The same technique has also been proposed for analysing the RSD signal and the combined BAO and RSD signal (Ruggeri et al. 2016; Zhao et al., in preparation). As future surveys will probe large volumes, covering wide ranges in redshift, we expect redshift weighting to be very useful. We plan on continuing to develop this approach in future work by applying it to existing surveys.

ACKNOWLEDGEMENTS

We would like to thank Will Percival for helpful conversations. This work was supported in part by the National Science Foundation under Grant no. PHYS-1066293 and the hospitality of the Aspen Center for Physics. NP and FZ are supported in part by a DOE Early Career Grant DE-SC0008080.

Funding for SDSS-III has been provided by the Alfred P. Sloan Foundation, the Participating Institutions, the National Science Foundation, and the US Department of Energy Office of Science. The SDSS-III website is http://www.sdss3.org/.

SDSS-III is managed by the Astrophysical Research Consortium for the Participating Institutions of the SDSS-III Collaboration including the University of Arizona, the Brazilian Participation Group, Brookhaven National Laboratory, Carnegie Mellon University, University of Florida, the French Participation Group, the German Participation Group, Harvard University, the Instituto de Astrofisica de Canarias, the Michigan State/Notre Dame/JINA Participation Group, Johns Hopkins University, Lawrence Berkeley National Laboratory, Max Planck Institute for Astrophysics, Max Planck Institute for Extraterrestrial Physics, New Mexico State University, New York University, Ohio State University, Pennsylvania State University, University of Portsmouth, Princeton University, the Spanish Participation Group, University of Tokyo, University of Utah, Vanderbilt University, University of Virginia, University of Washington, and Yale University.

Some of the codes in this paper made use of the Chapel programming language.[1]

[1] http://chapel.cray.com

REFERENCES

Alam S. et al., 2015, ApJS, 219, 12
Anderson L. et al., 2014, MNRAS, 441, 24
Beutler F. et al., 2011, MNRAS, 416, 3017
Blake C., Collister A., Bridle S., Lahav O., 2007, MNRAS, 374, 1527
Bond J. R., Efstathiou G., 1987, MNRAS, 226, 655
Carroll S. M., Press W. H., Turner E. L., 1992, ARA&A, 30, 499
Cole S. et al., 2005, MNRAS, 362, 505
Cuesta A. J. et al., 2016, MNRAS, 457, 1770
Dawson K. S. et al., 2013, AJ, 145, 10
Eisenstein D. J., Hu W., 1998, ApJ, 496, 605
Eisenstein D. J. et al., 2005, ApJ, 633, 560
Eisenstein D. J., Seo H.-J., White M., 2007, ApJ, 664, 660
Eisenstein D. J. et al., 2011, AJ, 142, 72
Hartlap J., Simon P., Schneider P., 2007, A&A, 464, 399
Hu W., Sugiyama N., 1996, ApJ, 471, 542
Kaiser N., 1987, MNRAS, 227, 1
Kazin E. A. et al., 2010, ApJ, 710, 1444
Landy S. D., Szalay A. S., 1993, ApJ, 412, 64
Lewis A., Challinor A., Lasenby A., 2000, ApJ, 538, 473
Nelder J. A., Mead R., 1965, Comput. J., 7, 308
Padmanabhan N., White M., 2008, Phys. Rev. D, 77, 123540
Padmanabhan N., Xu X., Eisenstein D. J., Scalzo R., Cuesta A. J., Mehta K. T., Kazin E., 2012, MNRAS, 427, 2132
Peebles P. J. E., Yu J. T., 1970, ApJ, 162, 815
Percival W. J. et al., 2010, MNRAS, 401, 2148
Percival W. J. et al., 2014, MNRAS, 439, 2531
Ruggeri R., Percival W., Gil-Marín H., Zhu F., Zhao G., Wang Y., 2016, preprint (arXiv:e-prints)
Seo H.-J., Eisenstein D. J., 2007, ApJ, 665, 14
Sunyaev R. A., Zeldovich Y. B., 1970, Ap&SS, 7, 3
Tegmark M., Taylor A. N., Heavens A. F., 1997, ApJ, 480, 22
White M., Tinker J. L., McBride C. K., 2014, MNRAS, 437, 2594
Xu X., Cuesta A. J., Padmanabhan N., Eisenstein D. J., McBride C. K., 2013, MNRAS, 431, 2834
Zhu F., Padmanabhan N., White M., 2015, MNRAS, 451, 236

APPENDIX A: EXPECTED VALUE OF $\langle\chi^2\rangle$

Consider the p-dimensional observations, $\boldsymbol{x}$. Each entry of $\boldsymbol{x}$ is a random variable with a Gaussian distribution with mean 0 and standard deviation 1, denoted as $x \sim \mathcal{N}(0, 1)$.

We compute the sample covariance matrix from d independent samples, $\boldsymbol{x}_i$ where $1 \leq i \leq d$,

$$\mathbf{C} = \frac{1}{d-1}\sum_{i=1}^{d}(\boldsymbol{x}_i)(\boldsymbol{x}_i)^t, \tag{A1}$$

where the superscript t is the transpose. An unbiased estimate of the precision matrix is then

$$\hat{\boldsymbol{\Psi}} = \left(1 - \frac{p+1}{d-1}\right)\mathbf{C}^{-1}. \tag{A2}$$

Note that both the covariance matrix $\mathbf{C}$ and precision matrix $\boldsymbol{\Psi}$ are $p \times p$ matrices.

The average χ^2 is given by

$$\langle\chi^2\rangle = \frac{1}{d}\sum_{i=1}^{d}\mathrm{tr}\left(\boldsymbol{x}_i^t\hat{\boldsymbol{\Psi}}\boldsymbol{x}_i\right) = \frac{1}{d}\sum_{i=1}^{d}\mathrm{tr}\left(\boldsymbol{x}_i\boldsymbol{x}_i^t\hat{\boldsymbol{\Psi}}\right). \tag{A3}$$

In the second equality, we have used the cyclic property of trace. Inserting equations (A1) and (A2) into equation (A3), we obtain the expected average χ^2 as

$$\langle\chi^2\rangle = \frac{1}{d}\mathrm{tr}\left((d-1)\mathbf{C}\hat{\boldsymbol{\Psi}}\right) \tag{A4}$$

$$= \frac{d-1}{d}\left(1 - \frac{p+1}{d-1}\right)p. \tag{A5}$$

The above calculation can be generalized for other distributions. The key message remains the same – that if we fit d independent samples by using the covariance matrix calculated from the same samples, the expected $\langle\chi^2\rangle$ and the degree-of-freedom p are related by equation (A5).

This paper has been typeset from a TEX/LATEX file prepared by the author.